Single-particle approach to many-body relaxation dynamics

Marta Pelc,[1] David Dams,[2] Abhishek Ghosh,[1] Miriam Kosik,[1] Marvin M. Müller,[2] Garnett Bryant,[3] Carsten Rockstuhl,[2] Andrés Ayuela,[4] and Karolina Słowik[1,*]

[1] *Institute of Physics, Nicolaus Copernicus University in Toruń, Grudziadzka 5, Toruń 87-100, Poland*
[2] *Institute of Theoretical Solid State Physics, Karlsruhe Institute of Technology (KIT), Karlsruhe 76131, Germany*
[3] *Joint Quantum Institute, University of Maryland and National Institute of Standards and Technology, College Park 20742, MD, USA; Nanoscale Device Characterization Division, National Institute of Standards and Technology, Gaithersburg 20899, MD, USA*
[4] *Centro de Física de Materiales, CFM-MPC CSIC-UPV/EHU, Paseo Manuel Lardizabal 5, Donostia-San Sebastián 20018, Spain; Donostia International Physics Center (DIPC), Paseo Manuel Lardizabal 4, Donostia-San Sebastián 20018, Spain*

(Dated: February 5, 2024)

This study addresses the challenge of modeling relaxation dynamics in quantum many-body systems, specifically focusing on electrons in graphene nanoflakes. While quantum many-body techniques effectively describe dynamics up to a few particles, these approaches become computationally intractable for large systems. Larger systems may be tackled with a single-particle approach that, however, struggles to incorporate relaxation effects. Existing relaxation models encounter issues such as an inability to capture system complexity and violation of the Pauli principle. In this work, we propose a novel single-particle model that accounts for various relaxation effects at the crossroads of quantum optics and solid-state photonics, that overcomes the limitations of previous models. Our approach is rooted in the quantum-optical Lindblad model, where relaxation rates are deactivated once the target levels saturate due to the Pauli principle. This approach is referred to as the saturated-Lindblad model. To validate the predictions of the saturated-Lindblad model, we confront them against phenomenological and many-body physics models in low-dimensional systems, including atomic chains and graphene nanoflakes. Remarkably, the saturated-Lindblad model exhibits excellent agreement with few-body calculations, distinguishing itself from other existing approaches. Moreover, by assigning different relaxation rates to different transitions, we successfully reproduce cascade de-excitation dynamics and predict emission spectra. The saturated-Lindblad model offers the ability to describe dynamics in systems of practical sizes, encompassing a wide range of structures that can be effectively captured within the single-particle description.

I. INTRODUCTION

When solving many-body problems in quantum mechanics, one struggles with the unfavorable scaling of the size of the many-body Hilbert space, being a tensor product of spaces of individual systems. In the exact diagonalization approach, a system of N_e fermions, each living in an N_H-dimensional Hilbert space, requires a description in the space of dimension of $\begin{pmatrix} N_H \\ N_e \end{pmatrix}$. This approach has been applied to various solid-state systems [1], including single- and multi-layered graphene [2–4] and atom chains[5]. However, as the size of the system grows beyond a few dozen particles, calculations become demanding and eventually impossible with state-of-the-art computers.

Graphene nanoflakes [6–11] are interesting for their tunable optical properties and hold promise for applications in modern optoelectronics. Practical, accurate modeling of the relaxation dynamics of graphene nanoflakes, involving thousands of electrons, motivates this work. In the tight-binding approximation, each of the carbon atoms forming the flake introduces three orbitals that hybridize in the sp^2 form, bonding in a honeycomb network, and an additional p_z orbital, with an electron that is to a good approximation free to move across the graphene lattice [12]. Including the spin degree of freedom, a flake of N carbon atoms has N p_z electrons on $2N$ orbitals, N being of the order of a few dozens to thousands for 1 to 10-nm-sized flakes. Rigorously modeling the many-body dynamics of such large structures requires substantial numerical effort and heavily limits the size of systems that can be treated.

Various approximation schemes to overcome the scaling problem have been devised from classical [13, 14] and quantum-corrected approaches [15, 16], to single-particle methods [17], including density functional theory [18] or Hartree-Fock [19], to many-body perturbation theory [20] and cluster expansion of the Bloch equations [21]. We propose an intermediate method between the time-dependent Hartree-Fock and the Markovian master equations, typically used in quantum optics. It is based on a single-particle approach. The actual many-body character of the system is accounted for *via* a nonlinear Coulomb Hamiltonian, in which the interactions between electrons are introduced through its density matrix dependence. Although the problem becomes nonlinear, the method allows tackling large flakes due to the linear scal-

* karolina@umk.pl

ing of the Hilbert space dimension with the system size [8, 9, 22, 23]. These systems naturally suffer from the dissipation of energy and coherence, which we will together refer to as *relaxation*. In the literature, relaxation in large systems is usually handled with a phenomenological approach, wherein the dissipation term forces the system towards a steady state which needs to be known in advance [8, 22, 24, 25].

A single-particle framework was introduced to model the electro-optical properties of graphene nanoflakes with adatoms in a recent work[26]. The adatoms are represented as two-level systems, the conventional model of quantum optics, while the graphene flake is a solid-state system acting as a scatterer. This framework allows studying optical phenomena in such hybrid structures, merging quantum optical and solid state perspectives. The coherent dynamics of the two systems can be combined within a tight-binding model of the flake augmented with the adatom orbitals. The dissipation of quantum-optical systems is typically described in the literature using the Lindblad model, while a phenomenological approach is applied in solid-state problems. Unfortunately, these models are hard to merge, and while each describes its part of the physics properly, they may inappropriately account for the other part of the hybrid system. Particular problems involve striking issues such as the Pauli principle violation and the inability to include different decay rates for various processes.

In this work, we propose a model that allows one to account for dissipation dynamics in many-body systems described within the single-particle framework. In this case, the traditional Lindblad approach misses the information on the number of particles that are described. Then, it may enforce population transfer to levels which are already fully occupied. Our model corrects this traditional approach with saturation effects which prevent violation of the Pauli principle. The model allows grasping the versatile relaxation effects at the intersection of quantum optics and solid-state photonics. The proposed model will be demonstrated for small atomic chains and graphene flakes, exploited currently in forefront research in the field of quantum plasmonics. The model's applicability extends to complicated systems tackled in the single-particle framework due to their complexity. Examples thereof are time-dependent atomistic descriptions of quantum dots, plasmonic nanoparticles, nanoscaled field-effect transistors, capacitors or nanocomposites. The atomistic structure has been shown to play an essential role in shaping the optical response of such systems [27–29] and to determine the character of optical resonances [30].

II. THEORY

The dynamics of a model atomic chain or graphene flake require following the evolution of an ensemble of N_e electrons. The electrons are identical in that the probability of occupying a given eigenstate of the flake is the same for each. The state of a given electron is thus a mixture of eigenstates, described with a single-particle time-dependent density matrix $\rho(t)$. Omitting the spin degree of freedom, the density matrix size $N \times N$ corresponds to N carbon atoms on the flake. An adatom attached to the flake may introduce additional orbitals, augmenting the Hilbert space size by the orbital number: for an adatom modeled as an N_a-level system, the Hilbert space dimension becomes $N_H = N + N_a$.

The dynamics of the density matrix is described by the single-particle master equation

$$\frac{\partial}{\partial t}\rho(t) = -\frac{i}{\hbar}\left[H, \rho(t)\right] - \mathcal{D}\left[\rho(t)\right]. \tag{1}$$

The Hamiltonian H in Eq. (1) describes the coherent part of the electronic evolution. Appendix B 1 describes its tight-binding form in the single-particle framework. Diagonalization of the tight-binding Hamiltonian yields a natural Hilbert space basis $\{|\varphi_j\rangle\}_{j=1}^{N_H}$ consisting of N_H energy eigenstates.

The relaxation term $\mathcal{D}\left[\rho(t)\right]$ considers effects related to energy dissipation or decoherence. The literature describes two distinct forms of this term, which we here refer to as *phenomenological* and *Lindblad* approaches. In the following, we discuss their forms and underlying approximations and compare their advantages and drawbacks. We view them in the context of a combination of the solid-state and quantum-optical perspectives to adequately model the hybrid system of flake and adatom, which are individually characterized by distinct relaxation mechanisms and rates.

A. Solid state perspective: phenomenological dissipation model

The phenomenological relaxation term has a relatively simple form and interpretation. It is commonly used to model a variety of ensemble systems with strong relaxation [8, 22, 24, 25]

$$\mathcal{D}\left[\rho(t)\right] = \gamma\left(\rho(t) - \rho^s\right). \tag{2}$$

The model characterizes all the relaxation processes with one parameter γ, which has the advantage of simplicity for the price of several approximations. The lifetime γ^{-1} sets the timescale at which the system evolves towards the stationary state ρ^s. For bulk graphene, the value of $\hbar\gamma \sim 1 - 10$ meV has been experimentally determined[24, 25, 31–33]. The model might be a good approximation for large graphene flakes. However, when applied to the hybrid system of flake and adatom, it prohibits including different dissipation rates for the adatom and the graphene flake, therefore being a rather coarse description from the atomic perspective and for a weak degree of hybridization between the atom and the flake.

Relaxation in bulk graphene and large flakes is dominated by electron-scattering- and phonon-induced decoherence [32]. However, other dissipation channels, particularly those related to the spontaneous emission of photons, become relevant for small systems and may lead to physically distinct behavior with an important role of population transfer in contrast to pure decoherence. This distinction is described in more detail below in the discussion of Lindblad operators. The simple phenomenological treatment ascribes the same timescales to these effects. Moreover, the treatment breaks the optical selection rules as it assigns the same transition rates to optically allowed and forbidden transitions.

The important property of the phenomenological model is that it forces the system back into its equilibrium state ρ^s. It is constructed according to the Aufbau principle:

$$\rho^s = \frac{1}{N_e} \sum_{j=1}^{N_e} |\varphi_j\rangle\langle\varphi_j|, \tag{3}$$

where N_e is the number of electrons on the flake and the orbitals are ordered by energy. By construction, the state includes the information on the many-electron character of the system and the Pauli blocking mechanism: Only one electron is allowed in one energy level as the spin degree of freedom is not included here. Note that we choose to normalize density matrices such that their trace is equal to 1 so that the diagonal elements represent the probabilities for an electron to occupy the basis states.

However, in quantum optics, the stationary state is usually unknown *a priori*. It results from a trade-off between the relaxation rates and the excitation strength, e.g., due to an electric field. For strong perturbations, saturation effects occur. The field influence on the equilibrium state is beyond the scope of the phenomenological approach, which is a good approximation for strongly dissipative systems, particularly for large flakes, as well as in the case of moderately strong illumination in the form of pulses shorter than the relaxation time γ^{-1}.

B. Quantum-optical perspective: Lindblad approach

A rigorous quantum-mechanical treatment of relaxation processes is based on the Lindblad equation [34, 35]:

$$\mathcal{D}\left[\rho(t)\right] = \sum_{k=1}^{N^2-1} \gamma_k \left(L_k \rho(t) {L_k}^\dagger - \frac{1}{2} \left\{ {L_k}^\dagger L_k, \rho(t) \right\} \right), \tag{4}$$

where γ_k are relaxation rates for processes described by Lindblad single-particle jump operators L_k. The index $k = \{i, j\}$ labels $N^2 - 1$ pairs of eigenstate indices. Two possible types of Lindblad operators can be distinguished:

- for $j \neq i$, the $N(N-1)$ jump operators $L_k \to \sigma_{ij} = |\varphi_i\rangle\langle\varphi_j|$ describe population transfer from the hybrid system's eigenstate $|\varphi_j\rangle$ to the eigenstate $|\varphi_i\rangle$ with the corresponding decay of coherence; spontaneous emission is related to transfer from higher to lower energy states, while optical pumping to transfer from lower to higher ones;

- for $j = i$, the $N - 1$ independent dephasing operators $L_k \to \sigma_{ii} = |\varphi_i\rangle\langle\varphi_i|$ which may arise, e.g., through inelastic electron scattering, and lead to decay of coherence without influencing the eigenstate populations. Note that for N eigenstates, there are N operators of this form. Any of these operators can be expressed in the form $|\varphi_i\rangle\langle\varphi_i| = \hat{\mathbb{1}} - \Sigma_{n\neq i}|\varphi_n\rangle\langle\varphi_n|$. Here, $\hat{\mathbb{1}}$ stands for the identity operator. Hence, the identity operator and $N - 1$ dephasing operators σ_{ii} are independent. Note that for the identity operator, $L_k = \hat{\mathbb{1}}$, the right-hand side of Eq. (4) is trivial.

For multilevel systems, relaxation rates corresponding to different operators must fulfill certain relations [36]. Each of the dissipation mechanisms above can be described with an independent rate γ_k, which allows assigning different rates to different processes. In particular, the adatom can be treated individually, e.g., selected dipole-forbidden transitions can be excluded. Furthermore, the rates of different allowed transitions can be specifically chosen, for example, evaluated according to the Weisskopf-Wigner theory.

However, there is a substantial drawback to the rigorous approach: Eq. (4) accounts for the relaxation of a many-body system under the condition that it is described in a corresponding Hilbert space. In the single-particle framework, $\rho(t)$ carries no information on the many-body character of the system. The price to pay is that the Pauli blocking mechanism is ignored in the master equation. The extreme manifestation of this fact is that spontaneous emission in the dissipation term (4) pushes the entire electronic population into the lowest-energy eigenstate of the system, severely violating the Pauli principle.

C. Saturated-Lindblad model

In addition to the previously introduced Lindblad formalism, we propose a saturated-Lindblad model. It aims to enable differentiating relaxation mechanisms and rates for processes involving different eigenstates of the hybrid system, as in the Lindblad approach, but at the same time, adhere to the Pauli principle. These goals are achieved by suppressing the energy dissipation rates from $|\varphi_i\rangle$ to $|\varphi_j\rangle$ as the population ρ_{jj} of the target state becomes fully occupied

$$\gamma_{ij} \to \gamma_{ij} \theta\left[1 - N_e \rho_{jj}(t)\right], \tag{5}$$

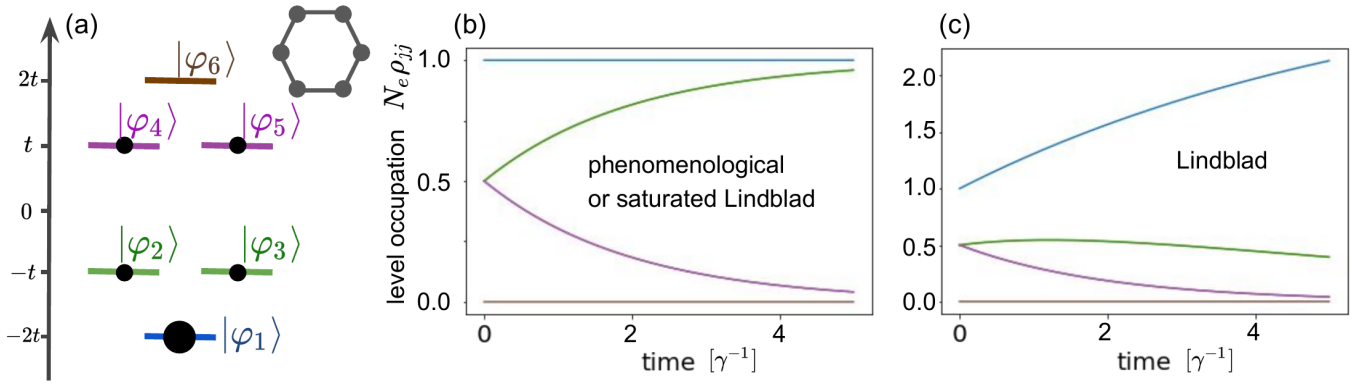

FIG. 1. (a) Tight-binding energy level scheme of a 6-atom ring. Black dots schematically depict the initial state population distribution [see Eq. (7)]. (b,c) Relaxation dynamics in a singly-excited benzene ring: (b) Identical curves for the phenomenological and saturated-Lindblad models with $\gamma_{ij} \equiv \gamma$ for all i, j. (c) Lindblad model. The line colors in panels (b,c) correspond to the colors marking the states in the level scheme in panel (a). Note that the unsaturated-Lindblad model violates the Pauli principle.

where

$$\theta(x) = \begin{cases} 0, & \text{for } x < 0, \\ 1, & \text{for } x \geq 0. \end{cases} \tag{6}$$

is the Heaviside function. For selected systems, we have compared the dynamics obtained by employing such a cutoff with dynamics in a model with a smooth saturation functional, avoiding the discontinuity of the Heaviside function. We find that the results obtained using the sharp Heaviside function best prevent the Pauli principle violation (see Appendix C). In the following section, we compare the relaxation dynamics obtained with different models with rigorous many-body simulations that can be made for small systems. Our results confirm the proper behavior of the proposed saturated model. Note that the spontaneous emission process is related to the population transfer from ρ_{ii} to ρ_{jj} with a rate γ_{ij} and the corresponding dephasing of the off-diagonal density matrix elements ρ_{ij} and ρ_{ji} with the rate $\frac{1}{2}\gamma_{ij}$. The process of pure dephasing related to the $|\varphi_i\rangle\langle\varphi_i|$ operators does not affect the population distribution, so the pure dephasing rate γ_{ii} is not constrained by the Pauli principle and it remains unsaturated in our model.

III. BENCHMARKING RESULTS

In this section, we discuss predictions of the relaxation models described above for five example cases. We start by examining electron dynamics in small systems with and without degeneracy. The example case of the 6-atom ring is used to demonstrate the unphysical dynamics predicted by the traditional unsaturated-Lindblad approach, already in the single-excitation case. The 6-atom chain example demonstrates different predictions of the phenomenological and saturated-Lindblad models for the case of a double excitation. The dynamics are directly compared to results obtained in the rigorous quantum-mechanical many-body approach. The latter is introduced in the Appendix B 2 and used as a benchmark. The following examples demonstrate the performance of the two models applied to larger systems and multiple excitations, which again lead to qualitatively different predictions of the dynamics and emission spectra. Finally, the difference in predicted dynamics is shown to be quantitatively increased in the presence of an adatom defect.

A. Benchmarking models: 3 electrons on a 6-atom ring

We first consider the relaxation dynamics for three electrons in a 6-atom ring using the tight-binding model with onsite energies set to zero (see the Hamiltonian in Appendix B 1). The ring has 6 single-particle eigenstates with energies $-2t$, $-t$, $-t$, t, t, $2t$, where t is the nearest-neighbor hopping rate. The Fermi energy of this system is zero due to electron-hole symmetry. The normalized ground state of the undoped system is constructed according to Eq. 3 that corresponds to the distribution of 1/3 of the electron population in each eigenstate below the Fermi energy. Figure 1 shows the relaxation dynamics for the single-excitation case with the initial state

$$\rho(t=0) = \frac{1}{3}\left(|\varphi_1\rangle\langle\varphi_1| + \frac{1}{2}\sum_{j=2}^{5}|\varphi_j\rangle\langle\varphi_j|\right), \tag{7}$$

schematically depicted in Fig. 1(a). With respect to the equilibrium state, half of the electronic population distributed at the degenerate energy level of $-t$ is now promoted to the energy level of t, with equal probabilities to occupy states $|\varphi_4\rangle$ and $|\varphi_5\rangle$. We have set all relaxation rates to the same value in the phenomenological case, and the original and saturated-Lindblad ones. This aspect is further discussed in Appendix D. The choice of

equal relaxation rates means that spontaneous emission among all pairs of states is possible. In contrast, decoherence may occur for all states except for the ground state. The phenomenological formalism generates an intuitive result, with the probabilities of states at the energy level t exponentially decaying and the occupation being transferred to the states at the energy level $-t$ [Fig. 1(b)]. Contrary, modeling the dynamics with the original Lindblad approach leads to a decay of the entire population of three electrons to the single-electron ground state $|\varphi_1\rangle$, clearly violating the Pauli principle [Fig. 1(c)]. This demonstrates the unphysical predictions of the Lindblad approach in the single-particle formalism applied to describe a many-body problem so that we can discard this model. Instead, the saturated-Lindblad model prevents the population drain to the single-particle ground state, reproducing exactly the results of the phenomenological model in panel (b). A many-body calculation with the model described in Appendix B 2 also fully confirms this behavior, exactly reproducing the curves in [Fig. 1(b)]. Appendix D explains the mathematical origin of this agreement. The accordance of the phenomenological and saturated-Lindblad results may not hold if a greater number of transitions is involved, as we demonstrate in the following example.

B. Benchmarking models: 3 electrons on a 6-atom chain

As a second example, we discuss the toy-model case of a 6-atom chain, for which ring degeneracies are lifted, and the three-electron ground state is given by Eq. 3 with $N_e = 3$. In the ground state, the highest-occupied orbital (HOMO) corresponds to the state $|\varphi_3\rangle$, while the lowest-unoccupied orbital (LUMO) – to state $|\varphi_4\rangle$ [Fig. 2(a)]. We consider three kinds of chains characterized by different sets of transition rates, shown in Fig. 2(b-d). The case with all relaxation rates being equal is considered to enable a direct comparison of the phenomenological and the saturated approaches: The phenomenological model assumes uniform transition rates regardless of the spatial structure of the system, transition frequencies, and dipole moments.

Two other important cases of linear atom chains are defined by the Su-Schrieffer-Heeger (SSH) model[37–40], whose tight-binding Hamiltonian is described in Appendix B 1. For SSH chains, the relaxation rates can be evaluated based on the Hamiltonian eigenstates according to the Weisskopf-Wigner formula[41]

$$\gamma_{ij} = \frac{\omega_{ij}^3 |\mathbf{d}_{ij}|^2}{3\pi\epsilon_0 \hbar c^3}. \tag{8}$$

Here, $\hbar\omega_{ij}$ is the transition energy between levels i and j, $\mathbf{d}_{ij}$ is the corresponding transition dipole moment, ϵ_0 is the vacuum permittivity, $\hbar$ stands for the reduced Planck constant, and c is the vacuum speed of light. Dipole moment elements are calculated as $\mathbf{d}_{ij} = -\langle\varphi_i|e\hat{\mathbf{r}}|\varphi_j\rangle = -e\sum_l a_{il}^\star a_{jl}\mathbf{r}_l$, where e is the elementary charge, a_{jl} are probability amplitudes for an electron described by the eigenstate $|\varphi_j\rangle$ to be localized at the carbon site l, and $\mathbf{r}_l$ is the site position. The values depicted in Fig. 2(c,d) for linear and dimer chains, have been normalized to the largest transition rate. Note that the calculated rates result from the Hamiltonian and include the properties of atomic orbitals and spatial positions of atoms. As the SSH chains are inversion symmetric, the eigenstates are either even or odd functions of electron positions. Selection rules forbid transitions between states of the same parity, which is reflected in the chess-like patterns of the evaluated Weisskopf-Wigner emission rates in Fig. 2(c,d). We can account for selection rules in the saturated-Lindblad approach, where we can introduce different transition rates and set those of dipole-forbidden transitions to 0.

We choose the initial state

$$\rho(t=0) = \frac{1}{3}\Big(|\varphi_1\rangle\langle\varphi_1| + |\varphi_2\rangle\langle\varphi_2| + \frac{1}{2}|\varphi_3\rangle\langle\varphi_3| + \frac{1}{2}|\varphi_4\rangle\langle\varphi_4|\Big), \tag{9}$$

which corresponds to the excitation of 50% of the HOMO population to the LUMO state. We again find excellent agreement between the phenomenological and saturated-Lindblad models, as we did for the ring and as is explained in Appendix D. We have an excellent agreement between models regardless of the chain relaxation rates because one LUMO – HOMO transition is active, which leads to exponential dynamics similar to the one shown in Fig.1(b).

We next consider cases where there are significant differences between the phenomenological and saturated-Lindblad modes, both in the time scale of the predicted relaxation dynamics and in which transitions are involved. More interesting is the case in which part of the initial HOMO population is transferred to the state $|\varphi_5\rangle$ (LUMO+1):

$$\rho(t=0) = \frac{1}{3}\Big(|\varphi_1\rangle\langle\varphi_1| + |\varphi_2\rangle\langle\varphi_2| + \frac{1}{2}|\varphi_3\rangle\langle\varphi_3| + \frac{1}{2}|\varphi_5\rangle\langle\varphi_5|\Big), \tag{10}$$

which is schematically depicted in the inset of Fig. 2(a). Intermediate transitions are now possible. For the chain with all relaxation rates equal $\gamma_{ij} = \gamma_{ii} = \gamma$ [Fig. 2(b)], we compare the results of the saturated-Lindblad and the phenomenological approaches in panels (e) and (f). The figure shows the population dynamics of the six eigenstates. According to the phenomenological model [panel (f)], the population is directly transferred from state $|\varphi_5\rangle$ to state $|\varphi_3\rangle$. Contrary, the saturated-Lindblad approach [panel (e)] leads to more physical behavior, with the population being transferred through the cascade from $|\varphi_5\rangle$ to $|\varphi_4\rangle$ to $|\varphi_3\rangle$, as expected. Note that the population of the decaying state $|\varphi_5\rangle$ is identical for both descriptions, as we have intentionally fitted the relaxation rate

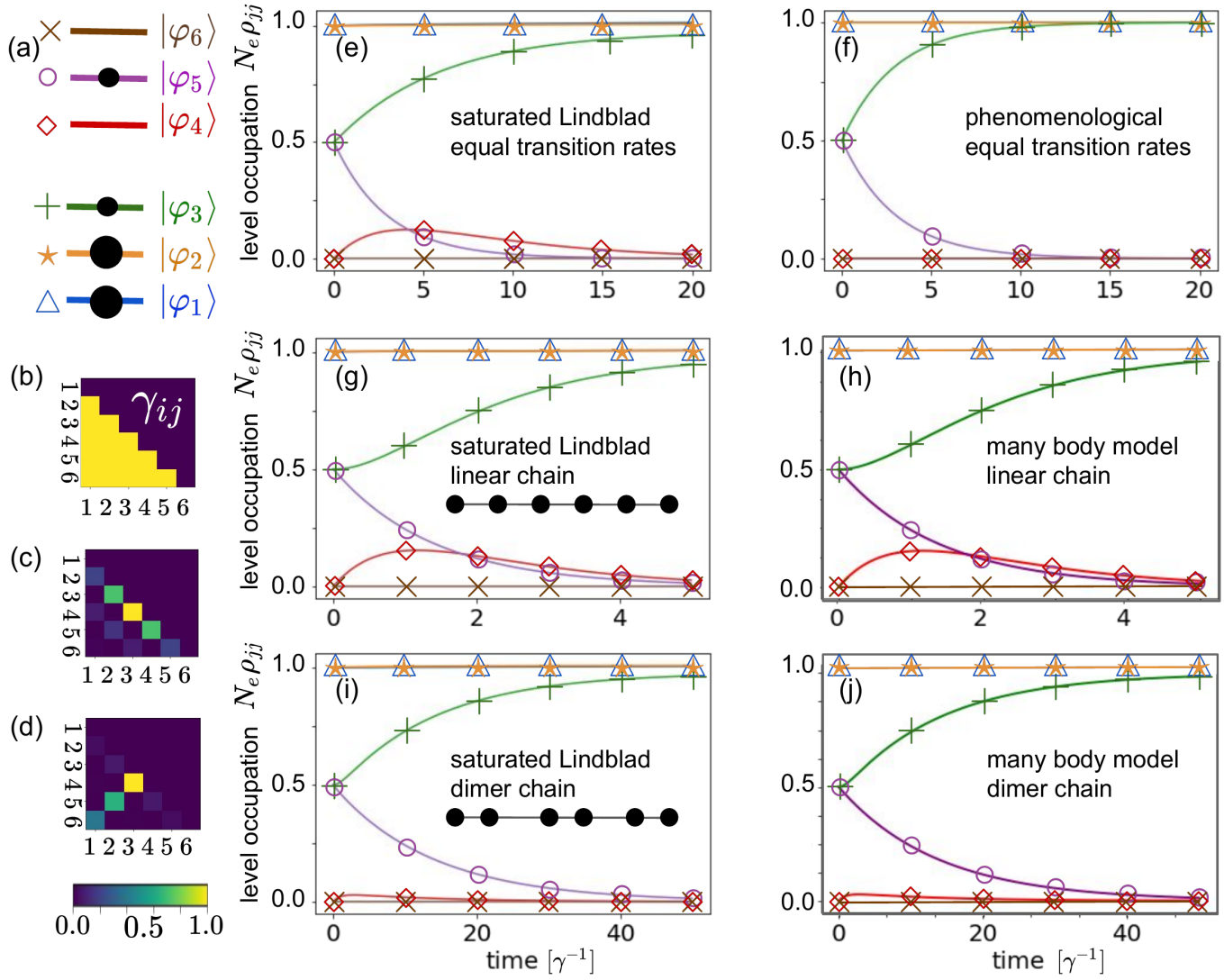

FIG. 2. Relaxation dynamics of doubly-excited six-atom chains. (a) Energy scheme in the single-electron approach. The single-electron eigenstates are not degenerate. The energy differences may vary for the linear chain, dimer chain, and chain with all transition rates equal.
(b,c,d) Colored arrays representing normalized transition rates γ_{ij}: the ij element of the array corresponds to a transition from $|\varphi_i\rangle$ to $|\varphi_j\rangle$ in a chain with all transition rates equal (b), a linear chain (c) and a dimer chain (d). The rates have been evaluated in the two latter cases according to the Weisskopf-Wigner formula (8).
(e,f) Relaxation dynamics for a chain with all transition rates equal: Expected level occupation $N_e\rho_{jj}$ in chain eigenstates modeled with the saturated-Lindblad (e) and phenomenological (f) approaches. (g,h) Relaxation dynamics for a linear chain: Expected level occupation $N_e\rho_{jj}$ in chain eigenstates modeled with the saturated-Lindblad (g) and many-body (h) approaches. (i,j) Same as (g,h) but for the dimer chain. Line colors and markers correspond to the eigenstates as depicted in panel (a). Note that the saturated-Lindblad model reproduces the many-body results very well.

in the phenomenological model. However, certain states remain unoccupied in the phenomenological model. This is a relevant difference: The cascade character of the saturated-Lindblad dynamics may imply longer evolution timescales, especially in larger systems involving more levels. In further examples, we will show how it leads to qualitatively different predictions of the emission spectra.

In panels (g-j) of Fig. 2, we display the results obtained for a linear chain and a dimer chain (for details, see Appendix B 1). Panels (g) and (i) have been obtained with the saturated-Lindblad approach, which yields clearly different relaxation dynamics in the two systems. Note that the dominant relaxation pathway in the linear chain occurs through a cascade of transitions between subsequent pairs of states [Fig. 2(c)]. In contrast, the transitions in the dimer chains occur between pairs of states that are symmetric with respect to the Fermi level [Fig. 2(d)]. This fact results in different evolution time scales on the horizontal axes of the plots. In the linear chain, the transition from $|\varphi_5\rangle$ to $|\varphi_4\rangle$ is rel-

atively quick and followed by the even faster transition from $|\varphi_4\rangle$ to $|\varphi_3\rangle$. In the dimer chain, the first transition occurs at a lower rate, and a longer time is needed for a considerable population transfer. Note that the selection rules in the linear and dimer chains reflect the metallic and semiconducting character of corresponding periodic chains. They can be used as toy models to understand the basic optical properties of larger systems, like graphene with its inter- and intraband transitions. Furthermore, note that the phenomenological model cannot capture the structural differences between the linear and dimer chains in real- or energy space: for a system of three electrons on six sites, the prediction of the phenomenological model is always the one shown in Fig. 2(f).

Panels (h) and (j) of Fig. 2 show the corresponding results obtained in the rigorous many-body approach for the case of three spinless electrons on six sites (see Appendix B 2 for details). We consider the agreement in the shape of the curves between the saturated-Lindblad and the many-body approach to be excellent because of the same time scales, the slopes of the curves, and the order in which the transitions occur. Note the results of the phenomenological model in panel (f) also fails to reproduce the features obtained with the rigorous approach.

For the 6-atom chain with 3 electrons, we have already found an order of magnitude speed-up in the computational time using the saturated-Lindblad approach compared to the many-body model. The computational cost scales quadratically with the system size, which scales linearly with the number of atoms in the single-particle approach and binomially with the number of electrons and atoms in the many-body case. For a system of 20 atoms with 10 electrons, the Hilbert space size becomes 20 in the single-particle approach, and $\begin{pmatrix} 20 \\ 10 \end{pmatrix} \sim 10^5$ in the many-body approach, with the estimated speed-up in the calculation time by the factor of 10^7 of the single-particle vs. many-body approaches. For a system of 100 atoms with 50 electrons, the Hilbert space sizes become 100 in the single-particle- or $\begin{pmatrix} 100 \\ 50 \end{pmatrix} \sim 10^{29}$ in the many-body approach, making the many-body calculations unreachable for state-of-the-art machines.

The excellent agreement between the proposed saturated-Lindblad model and the many-body calculations suggests that relaxation dynamics in many-body systems can be properly modeled with a single-particle approach, while still consuming reasonable computational time. This promises accurate calculations of many-body relaxation dynamics of complex, larger systems, relevant to novel optoelectronic applications of interest for quantum technologies, that would not be possible with traditional many-body approaches.

C. Scaling with the system size and emission spectra

We now investigate the mismatch between the predictions of the phenomenological model and the saturated-Lindblad model for the relaxation dynamics in larger systems. To do so, we study armchair-edged graphene flakes with 6, 18, and 36 carbon atoms (Fig. 3). The initial state population corresponds to one electron initially excited from the degenerate HOMO level (states $|\varphi_{\mathrm{H}}\rangle$, $|\varphi_{\mathrm{H+1}}\rangle$) to the LUMO+2 eigenstate $|\varphi_{\mathrm{L+2}}\rangle$, as represented by the size of the black dots in Fig. 3(a)

$$\rho(t=0) = \frac{1}{N_e}\left[\left(\sum_{j=1}^{\mathrm{H-2}} |\varphi_j\rangle\langle\varphi_j|\right) + \frac{1}{2}|\varphi_{\mathrm{H-1}}\rangle\langle\varphi_{\mathrm{H-1}}| + \frac{1}{2}|\varphi_{\mathrm{H}}\rangle\langle\varphi_{\mathrm{H}}| + |\varphi_{\mathrm{L+2}}\rangle\langle\varphi_{\mathrm{L+2}}|\right]. \tag{11}$$

All states below the HOMO-1 level are fully occupied. The transition rates for the saturated-Lindblad model are calculated using the Weisskopf-Wigner expression in Eq. (8). Their values are normalized to the largest among them and presented in arrays in Fig. 3(b-d) for increasing flake sizes. These graphs show symmetry with respect to the diagonal because of the electron-hole symmetry in graphene. Note the similarities of the structure of the relaxation rate arrays with those of the dimer chains shown above, which is related to the presence of two atomic sublattices. We find that as the size of the flake increases, the dynamics of electrons on the flakes seems to become similar between the two models [Fig. 3(e-g)]. This is because the main relaxation rate between the LUMO+2 and HOMO (HOMO -1) states are set equal in the two models. However, even for large flakes, the cascade character of the dynamics is reflected by the saturated-Lindblad model. This fact has important implications for light emission properties, as demonstrated by the emission spectra in Fig. 3(h-j), predicted by the two models. In spontaneous emission, the system relaxes from a higher-energy state $|\varphi_i\rangle$ to a lower-energy state $|\varphi_j\rangle$ with a time-dependent rate $\gamma_{ij}\rho_{ii}(t)$, emitting light with a Lorentzian spectral distribution[42]. We therefore construct the time-integrated spectra as sums of Lorentzian contributions

$$S(\omega) = \sum_{ij} \gamma_{ij} R_{ii} \frac{\gamma_{ij}}{(\omega-\omega_{ij})^2 + \gamma_{ij}^2}, \tag{12}$$

centered at the energies ω_{ij} of transitions allowed in the given model and broadened by the corresponding relaxation rates γ for the phenomenological model, and γ_{ij} from [Fig. 3(b-d)] for the saturated model. Each resonance is rescaled by the population $[R_{ii} = \int_0^{3\gamma_{\mathrm{LH}}^{-1}} dt\, \rho_{ii}(t)]$ of the state from which the emission occurs, integrated within the time interval three times the lifetime $\gamma_{\mathrm{LH}}^{-1}$ of the LUMO - HOMO transition. Figure 3(h-j) compares the spectra evaluated using the phenomenological (red solid line) and saturated-Lindblad approaches

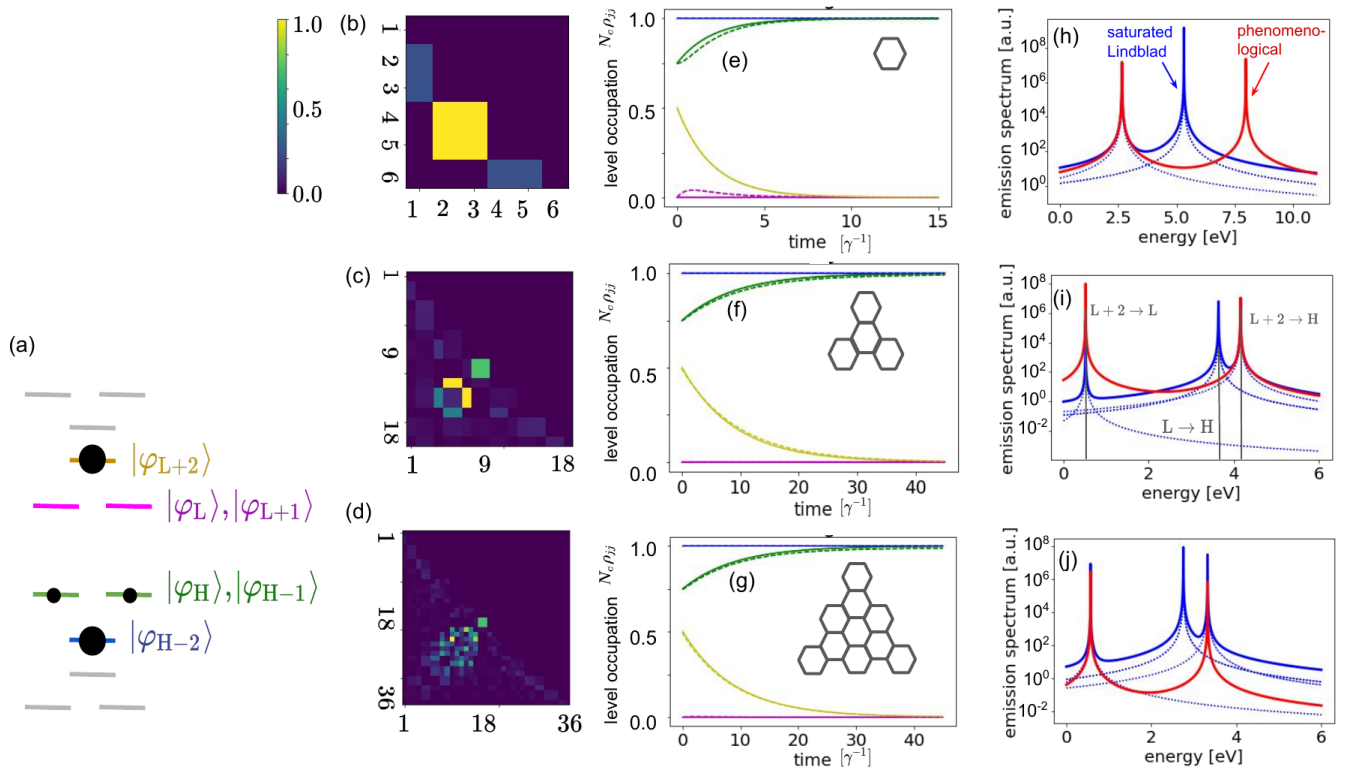

FIG. 3. (a) Energy scheme around the HOMO-LUMO gap of armchair-edged flakes with active levels marked in color, while other levels are shown in gray. The scheme of the 6-atom ring is limited to the states in color. (b-d) Weisskopf-Wigner relaxation rates from the states in different rows to the states in different columns for a 6-atom ring (b) and small graphene flakes (c,d). The rates have been normalized to the maximal value on each flake. (e-g) Relaxation dynamics on doubly-excited flakes for the phenomenological (solid lines) and saturated-Lindblad (dashed lines) models. Lines show populations of different color-encoded levels, according to the energy diagram given in panel (a). In the initial state, half of the HOMO/HOMO-1 level population (green) is excited to the LUMO+2 level shown in yellow. For the Lindblad model, relaxation rates are taken from the arrays in (b-d). For the phenomenological model, the rates are fit for the population of the decaying LUMO+2 (yellow) level to match the prediction of the saturated-Lindblad model. (h-j) Emission spectra for the three systems within the phenomenological (red solid lines) and saturated-Lindblad model (blue solid line). Blue dashed lines represent individual-transition contributions to the saturated-Lindblad spectrum. The three peaks correspond to the $|\varphi_{L+2}\rangle \to |\varphi_{L/L+1}\rangle$, $|\varphi_{L/L+1}\rangle \to |\varphi_{H/H-1}\rangle$ and $|\varphi_{L+2}\rangle \to |\varphi_{H/H-1}\rangle$ transitions, as indicated in panel (i). Note that despite the phenomenological model seems to reproduce well the dynamics as the size of the system is increased, it fails to reproduce the emission spectra.

(blue solid line). Additionally, we plot the individual resonances contributing to the saturated-model spectra with the blue dotted lines. For each investigated case, the phenomenological model predicts spectra with two equally broad peaks, representing the $|\varphi_{L+2}\rangle \to |\varphi_{L/L+1}\rangle$ and $|\varphi_{L+2}\rangle \to |\varphi_{H/H-1}\rangle$ transitions. This is because the LUMO/LUMO+1 level is unoccupied according to the phenomenological model. Hence, there can be no LUMO/LUMO+1 to HOMO/HOMO-1 transition. Contrary, three peaks are predicted by the saturated-Lindblad model, between the pairs $|\varphi_{L+2}\rangle \to |\varphi_{L/L+1}\rangle$, $|\varphi_{L/L+1}\rangle \to |\varphi_{H/H-1}\rangle$ and $|\varphi_{L+2}\rangle \to |\varphi_{H/H-1}\rangle$. The exception is the case of the 6-atom ring, for which the $|\varphi_{L+2}\rangle \to |\varphi_{H/H-1}\rangle$ transition is forbidden, and two peaks occur. The peaks may have different heights and widths in this model. Finally, we emphasize that the light emission dynamics would be correlated to the dynamics of the flakes. It implies that the saturated-Lindblad model predicts a sequence of bursts corresponding to the cascade transitions, while the phenomenological model rather suggests emission at both frequencies in parallel.

The role of the cascade transitions is emphasized as the system is initially excited to higher-energy states. We further illustrate this point in Fig. 4, considering the same 18-atom flake, initially with a 50% probability of occupation transfer from the HOMO to the highest-excited level [Fig. 4(a)]

$$\rho(t=0) = \frac{1}{9}\left[\left(\sum_{j=1}^{7}|\varphi_j\rangle\langle\varphi_j|\right) + \frac{3}{4}|\varphi_8\rangle\langle\varphi_8| + \frac{3}{4}|\varphi_9\rangle\langle\varphi_9| + \frac{1}{2}|\varphi_{18}\rangle\langle\varphi_{18}|\right]. \quad (13)$$

The relaxation dynamics are shown in Fig. 4(b). The cascade nature of the process with population transferred down the ladder of states is represented by the

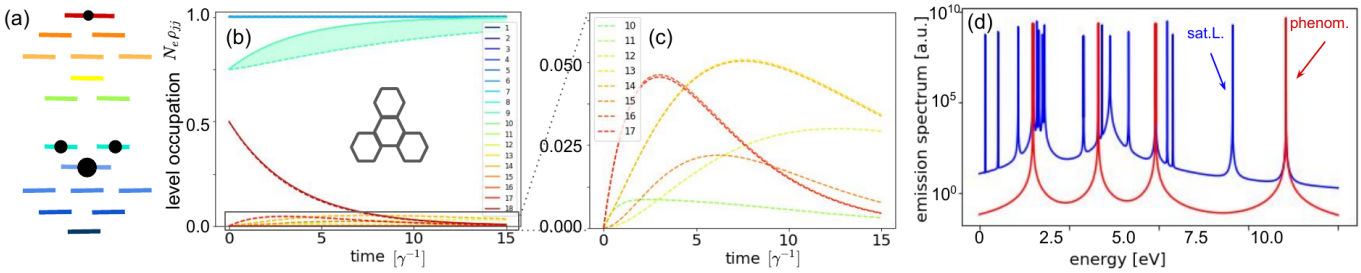

FIG. 4. (a) Energy scheme of an 18-atom armchair graphene flake with colors representing different levels. States shown in blue are all occupied with one electron. Two electrons are distributed between the states at the HOMO and the highest-excited level. (b) Relaxation dynamics in the system according to the phenomenological (solid lines) and saturated-Lindblad (dashed lines) models. Lines show populations of levels color-encoded in panel (a). Labels in the legend are indices of the eigenstates. The shaded area highlights the difference between the HOMO level occupation in the two models, which arises as a sum of the contributions of the subsequent states in the relaxation cascade. (c) Zoom on the population dynamics in the states contributing to the relaxation cascade in the saturated-Lindblad model. (d) Emission spectra based on the phenomenological (red) and saturated-Lindblad (blue) dynamics. Note that the phenomenological model neglects the cascade dynamics and the resulting structure of the emission spectra.

saturated-Lindblad model (dashed lines), contrary to the phenomenological model (solid lines) that predicts a direct transfer to the HOMO energy level. The agreement between the predictions of the two models becomes worse as the number of active transitions involved in the decay process is increased. The intermediate states contribute to the Lindblad dynamics [Fig. 4(c)], but they remain unpopulated in the phenomenological model. All of these populations sum up to a significant number, responsible for the difference in predicted populations of the HOMO level [cyan-shaded area in Fig. 4(b)]. This cascade dynamics leads to the rich emission spectra shown in Fig. 4(d) (blue line), different from the prediction of the phenomenological model (red line). The latter only captures the transitions from the initially excited state $|\varphi_{18}\rangle$. At the same time, the spectral structure predicted by the saturated-Lindblad model is much richer, accounting for all the contributing transitions.

D. Including an adatom

We now investigate how an adatom may influence the predictions of the dynamics within the two models. A two-level adatom with a single electron is attached to the edges of the same graphene flakes with 6, 18, and 36 carbon atoms. The adatom is coupled to a single carbon atom in each flake and is located in the plane, with a distance of 5.6 Å as depicted in the insets of Fig. 5(d-f). The energies of the isolated adatom ($\pm 0.38t$) are selected to lie in the HOMO-LUMO gap of the flake. (Here, $t = -2.66$ eV is the hopping parameter in graphene.) The hopping parameter between the adatom orbitals and its nearest-neighbor carbon atom $0.76t$ is slightly lower than in graphene. As a result, the adatom and the flake hybridize, and the energy spectra for different flake sizes are depicted in Fig. 5(a-c). The energy levels are plotted against the eigenstate number, and the marker colors indicate the fraction of the population localized at the adatom. The states marked in red originate at the adatom, while the dark blue ones are localized on the flake. The marker colors in between reflect the degree

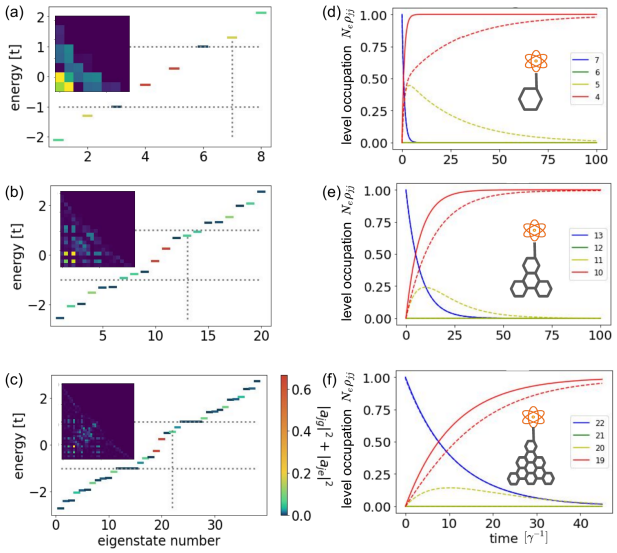

FIG. 5. Energy level schemes (a-c) and relaxation dynamics (d-f) of small graphene flakes with adatoms. The (a,d) panels correspond to a 6-atom ring; (b,e) – an 18 atom flake; (c,f) – a 36-atom flake with an adatom. Eigenstate energies in (a-c) are shown against the eigenstate number, while the colors indicate the localization $|a_{jg}|^2 + |a_{je}|^2$ of the eigenstate $|\varphi_j\rangle$ on the adatom, i.e., the fraction of population occupying its ground and excited states. The insets encode the relaxation rates in the Weisskopf-Wigner model. (d-f) Relaxation dynamics in the system according to the phenomenological (solid lines) and saturated-Lindblad (dashed lines) models. Numbers in the legend describe the eigenstate index. The phenomenological model of two coupled subsystems fails to reproduce trends even for the largest system size.

of hybridization between the two subsystems. Note that the HOMO state of the hybrid system is now mostly localized on the adatom and is indicated by the numbers 4, 10, or 19 for different flake sizes. The system is initialized in a state with an electron transferred from the HOMO state to the one indexed as LUMO+2. This state is chosen because it corresponds to the flake LUMO state hybridizing with the adatom. Spontaneous emission rates are evaluated according to the Weisskopf-Wigner theory. The transition dipole moment between the pair of isolated adatom eigenstates is set at $ea_0 = 1$ atomic unit, with a_0 being the Bohr radius. The dipole moment is oriented at 45 degrees relative to the horizontal direction in the figures, to couple with both basic orientations of the flake dipole moments.

As in previous examples, the phenomenological model shows a direct population transfer between a pair of levels [Fig. 5(d-f)]. On the other hand, the cascade nature of the population transfer is captured by the saturated-Lindblad approach. The difference in predictions of the two models is more significant than for isolated flakes investigated in Fig. 3 and clearly seen in Fig. 5(d-f). This difference arises due to the characteristic evolution timescales of the two subsystems that may significantly vary.

Furthermore, the presence of the adatom leads to spatial symmetry breaking of the system. The pair of states constituting the LUMO level of isolated flakes [e.g., the green level in Fig.4(a)] is two-fold degenerate. The presence of the adatom lifts this degeneracy. In consequence, the LUMO+2 state is hybridized with the adatom, and the LUMO+1 is decoupled. States LUMO+2 and LUMO+1 are states 7 and 6 in Fig. 5(a), 13 and 12 in (b), 22 and 21 in (c), respectively. LUMO+2 is marked with vertical dotted lines. Transitions involving the state denoted as LUMO+1 are dipole-forbidden, so this state plays little role in the relaxation dynamics. This illustrates that the system eigenstates may be modified because of the symmetry breaking by the adatom. The eigenstates are defined by the Hamiltonian, and hence, they are the same for both relaxation models. However, this symmetry breaking is further included in the saturated-Lindblad relaxation term, which accounts for the modified selection rules via different transition rates. Thus, the presence of the adatom may significantly influence the relaxation dynamics of the graphene flakes, which is accounted for by the saturated-Lindblad model. In fact, the lifetime of the LUMO state of the hybrid system may be longer than in pristine flakes, which could be of interest for experiments on graphene-based light emitters.

CONCLUSIONS

This study addresses the challenge of modeling the relaxation dynamics of quantum mechanical many-body systems using the single-particle approach. The saturated-Lindblad model introduced in this work successfully prevents the drain of the population to the single-particle ground state predicted by the treatment without saturation. Due to its simplicity, the phenomenological model cannot capture the optical selection rules, the richness of the cascade phenomena in relaxation dynamics or the complexity of the emission spectra.

The benchmark results with small-size many-body systems indicate that the saturated model effectively mimics the outcomes of the many-body calculations. This agreement enabled us to study large systems, such as pristine graphene flakes and flakes with adatoms. The model exhibits the expected cascade dynamics commonly explored in quantum optical technologies in the context of light emission. It is noteworthy that the model enables the assignment of different relaxation rates to different transitions and processes, in particular, taking into consideration the optical selection rules. Furthermore, it can capture the effects of symmetry breaking by the adatom, which can make forbidden transitions become bright with possibly distinct lifetimes. The proposed model may be important in engineering the emission properties of graphene-based optoelectronic devices and nanoscaled light emitters. In general, the model may encompass the quantum dynamics of diverse systems, including quantum dots, nanoscaled optoelectronic devices [43], light sources [44], plasmonic particles and 2D-materials-based nanocomposites [45].

Author contributions: All authors contributed to the concept, discussions, and the final version of the manuscript. M.K., M.M.M., and D.D. wrote the code for single-particle simulations. G.B. provided the many-body code, extended to dynamic simulations by A.A., M.P., and K.S. A.G. tested the codes. K.S. performed the simulations and wrote the first draft of the manuscript.

ACKNOWLEDGMENTS

A.G., M.P., and K.S. acknowledge support from the National Science Centre, Poland (Project No. 2020/39/I/ST3/00526). D.D. and C.R. acknowledge support by the German Research Foundation within the Project (RO 3640/14-1 under project number - 465163297). M.M.M. and C.R. acknowledge support by the German Research Foundation within the Project (RO 3640/8-1 under project number 378579271). A.A. acknowledges the support of the Spanish Ministry of Science and Innovation through grants PID2019-105488GB-I00 and TED2021-132074B-C32. We acknowledge financial support from the European Commission from the MIRACLE (ID 964450), NaturSea-PV (ID 101084348), and NRG-STORAGE project (GA 870114). The Basque Government supported this work through Project No. IT-1569-22. A.G., M.P., and K.S. are grateful to the Donostia International Physics Center for their kind hospitality.

Appendix A: Appendixes

Appendix B: Approaches to describe electrons on graphene flakes and atomic chains

1. Single-particle description

The tight-binding Hamiltonian for graphene flakes or atomic chains used as examples in this work takes the form

$$H = \sum_{\langle l,l' \rangle} t_{ll'} |l\rangle\langle l'|, \tag{B1}$$

where $|l\rangle$, $|l'\rangle$ stand for orbitals localized on atomic sites l and l', $t_{ll'} = t^{\star}_{l'l}$ is the hopping rate between the pair of orbitals, and the bracket $\langle \cdot, \cdot \rangle$ indicates a summation over the nearest-neighbors. For graphene, all hopping rates are taken to be equal $t_{ll'} \equiv t$. The nearest-neighbor model can naturally be extended without affecting the general conclusions of this work. The dimension of the Hamiltonian is equal to the number of sites. Therefore, this Hamiltonian can be diagonalized to determine the eigenstates $|\varphi_j\rangle$ and the corresponding energies ε_j.

For the one-dimensional SSH model of atomic chains, the single-particle tight-binding Hamiltonian (B1) can be rewritten as[37, 39, 40]

$$H_{\mathrm{TB}} = \sum_{l=1}^{N-1} \left[t + (-1)^{l-1} \Delta \right] \left(|l\rangle\langle l+1| + |l+1\rangle\langle l| \right). \tag{B2}$$

leading to an alternated coupling $t + \Delta$, $t - \Delta$ between subsequent pairs of atoms. In this work, we consider even numbers of atoms N. The case of $\Delta = 0$ corresponds to a linear chain with all nearest-neighbor hopping rates being equal, while the case of $\Delta > 0$ describes a dimer chain with alternate hoppings. In both cases, the inversion symmetry of the system is responsible for the symmetry of its eigenstates being even and odd functions of electron positions. Selection rules forbid transitions between states of the same parity. The results presented in Fig. 2 have been obtained for $\Delta = 0$ (the case of linear chain) and $\Delta = 0.3t$ (dimer chain). The optical properties of SSH chains have been described at length in Refs. [39, 40, 46].

2. Many-body description

The rigorous quantum-mechanical many-body approach allows for obtaining exact dynamics for small systems. It is based on the second quantization picture, in which the tight-binding Hamiltonian for a chain takes the form analogous to Eq. (B2), but is not limited to a single electron[37, 38, 47]

$$H_{\mathrm{mb}} = \sum_{l=1}^{N-1} \left[t + (-1)^{l-1} \Delta \right] \left(a_l^{\dagger} a_{l+1} + a_{l+1}^{\dagger} a_l \right). \tag{B3}$$

Here, the operator a_l annihilates an electron at site l. The operators obey the fermionic anticommutation rules $\{a_l, a_{l'}^{\dagger}\} = \delta_{ll'}$ and $\{a_l, a_{l'}\} = \{a_l^{\dagger}, a_{l'}^{\dagger}\} = 0$. This Hamiltonian preserves the number of excitations, hence, its eigenstates are simultaneously eigenstates of the total excitation number operator $\sum_l a_l^{\dagger} a_l$. Consequently, the problem can be solved independently in manifolds corresponding to fixed numbers of excitations (electrons) M, and the Hamiltonian can be rewritten in a block-diagonal form. The size of each block is the combinatorial number of possibilities to position M electrons on N lattice sites $\binom{N}{M}$, and the total Hamiltonian size is $\sum_{M=0}^{N} \binom{N}{M} = 2^N$ for each of the sites can be occupied or unoccupied by an electron. The Hamiltonian block corresponding to $M = 1$ of dimension N describes a single electron on a given lattice and takes the form given in Eq. (B1). Each Hamiltonian block can be independently diagonalized to yield M-body eigenstates $|\varphi_j^{(M)}\rangle$ within the given manifold. For $M = 1$ we drop the superscript in the state notation.

We restrict our analysis to relaxation processes that preserve the number of electrons. Then, a Lindblad operator can be independently defined for each manifold, where it takes the form analogous to the right-hand side of Eq. (4). However, the density matrix $\rho(t)$ and the Lindblad operators L_k describe the states and transitions in the given manifold and have its dimension $\binom{N}{M}$. The jump operators $L_k \to |\varphi_i^{(M)}\rangle\langle\varphi_j^{(M)}|$ describe a population transfer from a (higher-energy) state $|\varphi_j^{(M)}\rangle$ to a (lower-energy) state $|\varphi_i^{(M)}\rangle$, while operators $|\varphi_i^{(M)}\rangle\langle\varphi_i^{(M)}|$ are responsible for pure dephasing.

The master equation in the form of Eq. (1), rewritten for the M-body case, describes the dynamics of the M-body system. Since the size of the problem scales binomially with the number of sites and electrons, we make direct comparisons between the rigorous many-body approach and approximate single-particle models for small systems. The benchmark discussed in the main text considers a 3-electron case on a 6-site chain. The many-body Hilbert space is spanned by $\binom{6}{3} = 20$ eigenstates. Three of them are considered in the comparison:

$$|\varphi_1^{(M=3)}\rangle = b_1^{\dagger} b_2^{\dagger} b_3^{\dagger} |\mathrm{vac}\rangle, \tag{B4}$$

$$|\varphi_2^{(M=3)}\rangle = b_1^{\dagger} b_2^{\dagger} b_4^{\dagger} |\mathrm{vac}\rangle, \tag{B5}$$

$$|\varphi_3^{(M=3)}\rangle = b_1^{\dagger} b_2^{\dagger} b_5^{\dagger} |\mathrm{vac}\rangle. \tag{B6}$$

Here, the operators $b_j^{\dagger}$ create an excitation in the single-particle eigenstate $|\varphi_j\rangle$ and again, $\{b_j, b_{j'}^{\dagger}\} = \delta_{jj'}$ and $\{b_j, b_{j'}\} = \{b_j^{\dagger}, b_{j'}^{\dagger}\} = 0$. The symbol $|\mathrm{vac}\rangle$ represents the chain state without electrons. The energies of the many-body eigenstates are sums of the corresponding single-particle energies. Note that in the case of the linear

chain, there exists a state $|\varphi_4^{(M=3)}\rangle = b_1^\dagger b_3^\dagger b_4^\dagger|\text{vac}\rangle$ degenerate with $|\varphi_3^{(M=3)}\rangle$.

The many-body eigenstates represented in the compact second-quantization form in Eqs. (B4), can also be written in the form of Slater determinants, e.g.

$$|\varphi_1^{(M=3)}\rangle = \frac{1}{\sqrt{3!}} \begin{vmatrix} |\varphi_1\rangle_1 & |\varphi_2\rangle_1 & |\varphi_3\rangle_1 \\ |\varphi_1\rangle_2 & |\varphi_2\rangle_2 & |\varphi_3\rangle_2 \\ |\varphi_1\rangle_3 & |\varphi_2\rangle_3 & |\varphi_3\rangle_3 \end{vmatrix}, \tag{B7}$$

where $|\varphi_i\rangle_j$ denotes the orbital i describing electron j. The connection to the single-particle density matrices in the main text is made through a partial trace of an arbitrary pair of electrons. For example, the density matrix obtained through the partial trace of the many-body ground state is

$$\text{Tr}_{2,3}|\varphi_1^{(M=3)}\rangle\langle\varphi_1^{(M=3)}| = \text{Tr}_{3,1}|\varphi_1^{(M=3)}\rangle\langle\varphi_1^{(M=3)}| = \text{Tr}_{1,2}|\varphi_1^{(M=3)}\rangle\langle\varphi_1^{(M=3)}| = \frac{1}{3}\left(|\varphi_1\rangle\langle\varphi_1| + |\varphi_2\rangle\langle\varphi_2| + |\varphi_3\rangle\langle\varphi_3|\right), \tag{B8}$$

which is the special case of the equilibrium state in Eq. (3) for $N_e = 3$.

Many-body calculations in the main text, as shown in Fig. 2(h,j), have been performed for the linear or dimer chain initial state $\frac{1}{2}\left(|\varphi_1^{(M=3)}\rangle\langle\varphi_1^{(M=3)}| + |\varphi_3^{(M=3)}\rangle\langle\varphi_3^{(M=3)}|\right)$. This state is the many-body analogue of the single-particle state in Eq. (10) assumed to generate the dynamics in Fig. 2(e,f,g,i). With this initial state, the system evolves according to the many-body form of the master equation (1), where the density matrix describes the full three-electron system. The Hamiltonian is the three-electron block of H_{mb} in Eq. (B3). Relaxation is described within the traditional Lindblad approach in Eq.(4). The Lindblad operators L_k are given above, and the decay rates are set in accordance with the ones in the single-particle approach. As a result, we obtain the time-dependent three-electron 20×20 density matrix $\rho^{(3)}$. For the relaxation process, the states of energy higher than that of $|\varphi_3^{(M=3)}\rangle$ remain unoccupied, and the block spanned by $\{|\varphi_{k=1,2,3}^{(M=3)}\rangle\}$ has nonzero elements.

The level occupations $N_e\rho_{jj}$ in Fig. 2(e,f,g,i) are electron densities in the single-particle eigenstates $|\varphi_j\rangle$, normalized by the elementary charge. We use Eqs. (B4-B8) to evaluate the corresponding densities in the many-body framework. We note that the three-body state $b_{j_1}^\dagger b_{j_2}^\dagger b_{j_3}^\dagger|\text{vac}\rangle$ describes three electrons distributed among the three single-particle eigenstates $|\varphi_j\rangle$ with $j = j_1, j_2, j_3$. Due to the electron indistinguishability, each of the electrons occupies states $|\varphi_j\rangle$ with the probability of $\frac{1}{3}$ if $j \in \{j_1, j_2, j_3\}$ or 0 otherwise, as follows from Eq. (B8). Thus, the probability $P(|\varphi_j\rangle)$ that an arbitrary electron occupies the single-particle eigenstate $|\varphi_j\rangle$ takes the conditional form:

$$P(|\varphi_j\rangle) = \sum_{k=1,2,3} \rho_{kk}^{(3)} p_j^k. \tag{B9}$$

The element $\rho_{kk}^{(3)}$ is the probability of the system to be found in the three-electron state $|\varphi_k^{(M=3)}\rangle$, and $p_j^k \in \{0, \frac{1}{3}\}$ is the probability of an electron to occupy the single-particle eigenstate $|\varphi_j\rangle$ given that the system is in $|\varphi_k^{(M=3)}\rangle$. The normalized charge densities or single-particle level occupations are obtained through the multiplication of $P(|\varphi_j\rangle)$ by the total number of electrons being $N_e = 3$. We obtain for the occupations of subsequent levels:

$$P(|\varphi_1\rangle) = 3\sum_{k=1,2,3} \rho_{kk}^{(3)} \frac{1}{3} = 1, \tag{B10}$$

$$P(|\varphi_2\rangle) = 3\sum_{k=1,2,3} \rho_{kk}^{(3)} \frac{1}{3} = 1, \tag{B11}$$

$$P(|\varphi_3\rangle) = 3\rho_{11}^{(3)} \frac{1}{3} = \rho_{11}^{(3)}, \tag{B12}$$

$$P(|\varphi_4\rangle) = 3\rho_{22}^{(3)} \frac{1}{3} = \rho_{22}^{(3)}, \tag{B13}$$

$$P(|\varphi_5\rangle) = 3\rho_{33}^{(3)} \frac{1}{3} = \rho_{33}^{(3)}, \tag{B14}$$

$$P(|\varphi_6\rangle) = 0. \tag{B15}$$

These quantities are shown in Fig. 2(h,j).

Appendix C: Smooth saturating functional

The proposed saturated-Lindblad model involves an abrupt cutoff of the relaxation channels to avoid transferring the population to fully occupied states for which $N_e\rho_{jj} = 1$. We herein consider a smoother suppression of the energy dissipation rates from $|\varphi_i\rangle$ to $|\varphi_j\rangle$ as the population ρ_{jj} of the target state approaches the Pauli limit of 1 electron per eigenstate: $\gamma_{ij} \to \gamma_{ij} S\left[\rho_{jj}(t)\right]$, where the saturating functional is given by

$$S\left[\rho_{jj}(t)\right] = \frac{1}{2}\left\{1 - \frac{\tan^{-1}\left[\, m(N_e\rho_{jj}(t) - 1)\right]}{\tan^{-1} m}\right\}. \tag{C1}$$

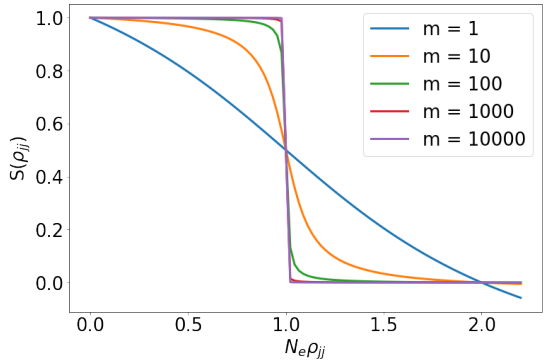

FIG. A.1. Saturating function $S(x)$ for various multipliers m.

The multiplier m allows one to control the smoothness of the saturating functional (Fig. A.1) that in the $m \to \infty$ limit becomes the theta function $\theta(1-N_e\rho_{jj}(t))$. This choice involves an arbitrary multiplier m. The corresponding shapes of the saturation function are shown in Fig. A.1. Figure A.2 shows how the level occupations are modified for different choices of the multiplier. The dynamics of the system is well modeled for large multipliers.

Appendix D: Discussion of relaxation rates in the phenomenological and saturated-Lindblad models

The Weisskopf-Wigner theory provides a recipe to evaluate the spontaneous emission rates for quantum transitions in the electric-dipole approximation. On the other hand, the decoherence rate in graphene can be experimentally determined. A comparison of the results obtained for bulk graphene [24, 48–50] and graphene quantum dots [51, 52] reveals a size dependence, in accordance with the expectation that decoherence is reduced in small quantum systems. In this appendix, we investigate conditions in which the phenomenological and saturated-Lindblad approaches converge to the same timescales in dynamics. The analysis additionally helps us understand how the phenomenological relaxation rate, known from experiments, should be modified in small flakes.

The dynamics of a density matrix element in the phenomenological approach follow straightforwardly from Eq. (2)

$$\dot{\rho}_{mn} = -\gamma(\rho_{mn} - \rho^s_{mn}). \tag{D1}$$

For the Lindblad evolution, we first discuss the nondegenerate case without saturation. To include saturation, selected rates can be set to 0. Let us first consider the evolution induced by the jump operators $|\varphi_j\rangle\langle\varphi_k|$ for the density matrix elements ρ_{mn} in the basis of system eigenstates:

$$\dot{\rho}_{mm} = \sum_{k>m} \gamma_{km}\rho_{kk} - \rho_{mm}\sum_{k<m}\gamma_{mk}, \tag{D2}$$

$$\dot{\rho}_{mn} = -\frac{1}{2}\rho_{mn}\left(\sum_{k<m}\gamma_{mk} + \sum_{k<n}\gamma_{nk}\right), \tag{D3}$$

where we have inserted the jump dissipation operators given above in the Lindblad equation (4). The first equation holds for the diagonal elements and describes the inflow of the population from the states energetically above $|\varphi_m\rangle$ and its outflow to the states energetically below. The other equation demonstrates that the off-diagonal elements decohere with the collective rate induced by all contributing transitions. We repeat the calculation for the dephasing operators $|\varphi_k\rangle\langle\varphi_k|$ to obtain

$$\dot{\rho}_{mm} = 0, \tag{D4}$$

$$\dot{\rho}_{mn} = -\frac{1}{2}\left(\gamma_m + \gamma_n\right)\rho_{mn}. \tag{D5}$$

Let us now discuss the simple initial state with a single excitation from the HOMO to the LUMO state, and relaxation back to the equilibrium. Then, the only unsaturated transition is from LUMO to HOMO, and we obtain the relaxation dynamics of the populations:

$$\dot{\rho}_{\mathrm{LL}} = -\gamma\rho_{\mathrm{LL}}, \tag{D6}$$

$$\dot{\rho}_{\mathrm{HH}} = +\gamma\rho_{\mathrm{LL}}, \tag{D7}$$

and $\dot{\rho}_{mn} = 0$ otherwise. The exact same form of equations is found in the phenomenological case with the stationary density matrix corresponding to the equilibrium distribution $\rho^s_{ii} = \frac{1}{N}$. This happens since for the HOMO state $\Delta\rho_{\mathrm{HH}} = \rho_{\mathrm{HH}} - \frac{1}{N} = -\rho_{\mathrm{LL}}$. This explains the perfect agreement of results obtained for the case of single-excitation in the 6-atom ring [Fig. 1(b)] or chain, discussed under Eq. (9).

In relatively large systems, higher excitations can be considered around the HOMO-LUMO gap with $m, n \approx \frac{N}{2}$, N being the large number of atoms forming the flake. Let us assume an initially excited state with the index m. The states above $|\varphi_m\rangle$ are usually empty, i.e., $\rho_{ii} = 0$ for $i > m$. Now, if we assume all equal transition rates, we obtain

$$\dot{\rho}_{mm} = -\frac{N\gamma}{2}\rho_{mm}, \tag{D8}$$

$$\dot{\rho}_{mn} \approx -\frac{N\gamma}{2}\rho_{mn}. \tag{D9}$$

The decay rate of the initially excited state becomes $N\gamma$, which can be reproduced in the phenomenological model in Eq. (2) with the replacement $\gamma \to N\gamma$. Indeed, in the examples, we have fitted the phenomenological decoherence rate to match the decay rate of the initially excited state. Note however that the dynamics of the target-level occupations are not well reproduced phenomenologically as the cascade dynamics is not captured.

The above estimation demonstrates how in large systems the overall relaxation rate increases with system

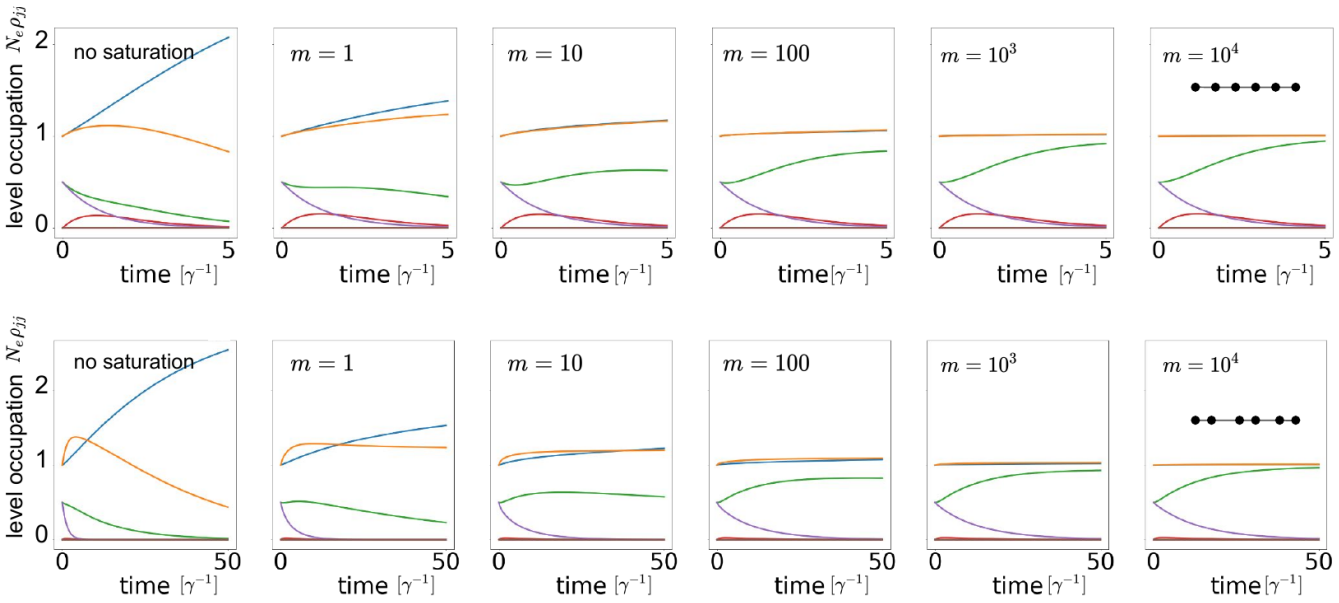

FIG. A.2. Impact of the multiplier m in the saturation function $S(\rho)$ in Eq. (C1) on the modeled relaxation dynamics in 6-atom linear (top row) and dimer (bottom row) chains. The left panels show the results obtained for the unsaturated-Lindblad model. The right panel approaches the limiting results already presented in Fig. 2(g,i).

size. This observation goes along with the expectation that larger systems relax faster. To explain the finite relaxation rate in bulk graphene, we consider a fragment of the sheet of the size of graphene coherence length $l_{\rm coh}$. At low temperatures, $l_{\rm coh} \sim 1$ μm [53, 54]. Then, the carbon atoms within a circle of radius $l_{\rm coh}$ contribute to the decoherence of the atoms in its center. The number $N_{\rm coh}$ of contributing atoms can be estimated as the ratio of the coherence circle area and the hexagon area in graphene, being the area per atom

$$N_{\rm coh} \sim \left(\frac{l_{\rm coh}}{a_{\rm cc}}\right)^2 \approx 10^7, \tag{D10}$$

where $a_{\rm cc} \approx 1.42$ Å is the carbon-carbon distance in graphene. Bulk-graphene decoherence rate $\gamma_{\rm bulk} \approx 10$ THz [24, 48–50] is mostly related to inelastic electron scattering. The above result suggests that its contribution "per transition" (or "per atom") might be comparable to the spontaneous emission rate of the LUMO-HOMO transition, which in small flakes with band gaps in the optical to the near-infrared regime is of the order of a few MHz. In larger systems, decoherence scales linearly with the number of atoms as shown above, while the spontaneous emission decreases proportionally to the third power of the band gap energy. This means that phonon-induced decoherence is expected to dominate in flakes of sizes of several thousand atoms or larger.

[1] H. Bruus and K. Flensberg, *Many-body quantum theory in condensed matter physics: an introduction* (OUP Oxford, 2004).

[2] S. D. Sarma, E. Hwang, and W.-K. Tse, Many-body interaction effects in doped and undoped graphene: Fermi liquid versus non-fermi liquid, Phys. Rev. B **75**, 121406(R) (2007).

[3] S. Das Sarma, S. Adam, E. Hwang, and E. Rossi, Electronic transport in two-dimensional graphene, Rev. Mod. Phys. **83**, 407 (2011).

[4] S. Yuan, R. Roldán, and M. I. Katsnelson, Excitation spectrum and high-energy plasmons in single-layer and multilayer graphene, Phys. Rev. B **84**, 035439 (2011).

[5] E. Townsend, T. Neuman, A. Debrecht, J. Aizpurua, and G. W. Bryant, Many-body physics in small systems: Observing the onset and saturation of correlation in linear atomic chains, Phys. Rev. B **103**, 195429 (2021).

[6] I. Snook and A. Barnard, Graphene nano-flakes and nano-dots: Theory, experiment and applications, in *Physics and Applications of Graphene*, edited by S. Mikhailov (IntechOpen, Rijeka, 2011) Chap. 13.

[7] A. Kuc, T. Heine, and G. Seifert, Structural and electronic properties of graphene nanoflakes, Phys. Rev. B **81**, 085430 (2010).

[8] J. D. Cox and F. Javier García de Abajo, Electrically tunable nonlinear plasmonics in graphene nanoislands, Nat. Commun. **5**, 5725 (2014).

[9] J. D. Cox, A. Marini, and F. J. G. De Abajo, Plasmon-assisted high-harmonic generation in graphene, Nat. Commun. **8**, 14380 (2017).

[10] A. Pizzi, G. Rosolen, and L. J. Wong et al., Graphene metamaterials for intense, tunable, and compact extreme ultraviolet and X-Ray sources, Adv. Science **7**, 1901609 (2020).

[11] F. Aguillon and A. G. Borisov, Atomic-scale defects might determine the second harmonic generation from plasmonic graphene nanostructures, J. Phys. Chem. Lett. **14**, 238 (2023).

[12] P. R. Wallace, The band theory of graphite, Phys. Rev. **71**, 622 (1947).

[13] R. Yu, J. D. Cox, J. Saavedra, and F. J. García de Abajo, Analytical modeling of graphene plasmons, ACS Photonics **4**, 3106 (2017).

[14] A. Pitilakis and E. E. Kriezis, Graphene optical nonlinearity: From the third-order to the non-perturbative electrodynamic regime, arXiv preprint arXiv:2203.09373 (2022).

[15] G. Toscano, J. Straubel, A. Kwiatkowski, C. Rockstuhl, F. Evers, H. Xu, N. Asger Mortensen, and M. Wubs, Resonance shifts and spill-out effects in self-consistent hydrodynamic nanoplasmonics, Nature communications **6**, 7132 (2015).

[16] N. A. Mortensen, Mesoscopic electrodynamics at metal surfaces, Nanophotonics **10**, 2563 (2021).

[17] B. Cui, M. Sukharev, and A. Nitzan, Comparing semiclassical mean-field and 1-exciton approximations in evaluating optical response under strong light–matter coupling conditions, The Journal of chemical physics **158** (2023).

[18] W. Kohn and L. J. Sham, Self-consistent equations including exchange and correlation effects, Phys. Rev. **140**, A1133 (1965).

[19] A. Szabo and N. Ostlund, *Modern Quantum Chemistry: Introduction to Advanced Electronic Structure Theory*, Dover Books on Chemistry (Dover Publications, 1996).

[20] L. Reining, The GW approximation: content, successes and limitations, Wiley Interdisciplinary Reviews: Computational Molecular Science **8**, e1344 (2018).

[21] M. Kira and S. Koch, *Semiconductor Quantum Optics* (Cambridge University Press, 2011).

[22] M. M. Müller, M. Kosik, and M. Pelc et al., Energy-based plasmonicity index to characterize optical resonances in nanostructures, J. Phys. Chem. C **124**, 24331 (2020).

[23] M. M. Müller, M. Kosik, and M. Pelc et al., From single-particle-like to interaction-mediated plasmonic resonances in graphene nanoantennas, J. Appl. Phys. **129**, 093103 (2021).

[24] H. Wang, J. H. Strait, and P. A. George et al., Ultrafast relaxation dynamics of hot optical phonons in graphene, Appl. Phys. Lett. **96**, 081917 (2010).

[25] M. Breusing, S. Kuehn, and T. Winzer et al., Ultrafast nonequilibrium carrier dynamics in a single graphene layer, Phys. Rev. B **83**, 153410 (2011).

[26] M. Kosik, M. M. Müller, and K. Słowik et al., Revising quantum optical phenomena in adatoms coupled to graphene nanoantennas, Nanophotonics **11**, 3281 (2022).

[27] S. Thongrattanasiri, A. Manjavacas, and F. J. García de Abajo, Quantum finite-size effects in graphene plasmons, ACS Nano **6**, 1766 (2012).

[28] P. Zhang, J. Feist, A. Rubio, P. García-González, and F. García-Vidal, Ab initio nanoplasmonics: The impact of atomic structure, Phys. Rev. B **90**, 161407(R) (2014).

[29] M. Barbry, P. Koval, and F. Marchesin et al., Atomistic near-field nanoplasmonics: reaching atomic-scale resolution in nanooptics, Nano Lett. **15**, 3410 (2015).

[30] R. L. Gieseking, Plasmons: untangling the classical, experimental, and quantum mechanical definitions, Materials horizons **9**, 25 (2022).

[31] C. H. Lui, K. F. Mak, J. Shan, and T. F. Heinz, Ultrafast photoluminescence from graphene, Phys. Rev. Lett. **105**, 127404 (2010).

[32] I. Gierz, J. C. Petersen, and M. Mitrano et al., Snapshots of non-equilibrium Dirac carrier distributions in graphene, Nat. Materials **12**, 1119 (2013).

[33] M. Slota, A. Keerthi, and W. K. Myers et al., Magnetic edge states and coherent manipulation of graphene nanoribbons, Nature **557**, 691 (2018).

[34] V. Gorini, A. Kossakowski, and E. C. G. Sudarshan, Completely positive dynamical semigroups of n-level systems, J. Math. Phys. **17**, 821 (1976).

[35] G. Lindblad, On the generators of quantum dynamical semigroups, Commun. Math. Phys. **48**, 119 (1976).

[36] S. G. Schirmer and A. I. Solomon, Constraints on relaxation rates for n-level quantum systems, Phys. Rev. A **70**, 022107 (2004).

[37] W. Su, J. Schrieffer, and A. Heeger, Solitons in polyacetylene, Phys. Rev. Lett. **42**, 1698 (1979).

[38] B. Pérez-González, M. Bello, Á. Gómez-León, and G. Platero, Interplay between long-range hopping and disorder in topological systems, Phys. Rev. B **99**, 035146 (2019).

[39] S. de Vega, J. D. Cox, F. Sols, and F. J. García de Abajo, Strong-field-driven dynamics and high-harmonic generation in interacting one dimensional systems, Phys. Rev. Research **2**, 013313 (2020).

[40] M. M. Müller, M. Kosik, M. Pelc, G. W. Bryant, A. Ayuela, and K. Rockstuhl, Carsten ad Słowik, Modification of the optical properties of molecular chains upon coupling to adatoms, Phys. Rev. B **104**, 235414 (2021).

[41] M. Scully and M. Zubairy, *Quantum Optics*, Quantum Optics (Cambridge University Press, 1997).

[42] R. Loudon, *The Quantum Theory of Light* (OUP Oxford, 2000).

[43] A. R.-P. Montblanch, M. Barbone, I. Aharonovich, M. Atatüre, and A. C. Ferrari, Layered materials as a platform for quantum technologies, Nature Nanotech. , 1 (2023).

[44] R. Khelifa, S. Shan, A. J. Moilanen, T. Taniguchi, K. Watanabe, and L. Novotny, WSe2 light-emitting device coupled to an h-BN waveguide, ACS Photonics (2023).

[45] A. Qadir, T. K. Le, and M. Malik et al., Representative 2d-material-based nanocomposites and their emerging applications: A review, RSC Advances **11**, 23860 (2021).

[46] J. Kim and W. Su, Quantum lattice motion and optical properties of polyenes, Synthetic Metals **49**, 83 (1992).

[47] J. K. Asbóth, L. Oroszlány, and A. Pályi, *A Short Course on Topological Insulators: Band Structure and Edge States in One and Two Dimensions* (Springer, 2016) pp. 1–22.

[48] K. S. Novoselov, A. K. Geim, and S. V. Morozov et al., Electric field effect in atomically thin carbon films, Science **306**, 666 (2004).

[49] K. S. Novoselov, A. K. Geim, and S. V. Morozov et al., Two-dimensional gas of massless Dirac fermions in graphene, Nature **438**, 197 (2005).

[50] M. Jablan, H. Buljan, and M. Soljačić, Plasmonics in graphene at infrared frequencies, Phys. Rev. B **80**, 245435 (2009).

[51] C. Volk, C. Neumann, and S. Kazarski et al., Probing relaxation times in graphene quantum dots, Nat. Commun. **4**, 1753 (2013).

[52] M. L. Mueller, X. Yan, J. A. McGuire, and L.-s. Li, Triplet states and electronic relaxation in photoexcited graphene quantum dots, Nano Lett. **10**, 2679 (2010).

[53] S. V. Morozov, K. S. Novoselov, M. Katsnelson, F. Schedin, L. Ponomarenko, D. Jiang, and A. Geim, Strong suppression of weak localization in graphene, Phys. Rev. Lett. **97**, 016801 (2006).

[54] K. Kechedzhi, D. Horsell, F. Tikhonenko, A. Savchenko, R. Gorbachev, I. Lerner, and V. Falko, Quantum transport thermometry for electrons in graphene, Phys. Rev. Lett. **102**, 066801 (2009).